Letters

An Analytical Stray Capacitance Model of NiZn Inductors With Gapped Cores

Zhan Shen, *Senior Member, IEEE*, Qiming Liu, Kaiyuan Liu, Yueyin Wang, Wu Chen, *Senior Member, IEEE*, Jingxin Hu, Yuefei Zuo, Frede Blaabjerg, *Fellow, IEEE*, and Huai Wang, *Senior Member, IEEE*

***Abstract*—NiZn cores are widely used in magnetic components in power electronic converters at frequencies above MHz, and the parasitic capacitance generated by air gaps in the cores of inductors can contribute to current ringing and electromagnetic interference (EMI) issues, which cannot be ignored during inductor modeling and design. Current research on air gap capacitance mainly focuses on MnZn materials and can cause significant errors when applied for NiZn materials. In this article, two models for stray capacitance of air gaps in NiZn cores are proposed. The boundary potential condition is derived by two methods to calculate the electric field distribution and energy capacitance stored in the air gaps. The model can calculate air gaps with different positions, numbers, sizes, and boundary conditions. Simulation and experimental verifications are carried out in six cases of gapped core inductors, and the average error of the air gap capacitance is approximately 13.2%.**

***Index Terms*—Air gap, electric field distribution, high-frequency magnetics, inductor, NiZn ferrite, stray capacitance.**

I. Introduction

THE wide adoption of third-generation semiconductors, particularly SiC and GaN, drives the switching frequency of power electronic converters to be progressively elevated, leading to the miniaturization in converter volume and intensified capacitive coupling within magnetics [1]. Such enhanced coupling induces high-frequency oscillations and electromagnetic interference (EMI) issues, which may jeopardize insulation and converter reliability [2]. Precise capacitance models are essential for mitigating high-frequency oscillations and achieving optimized converter design.

Received 5 September 2025; revised 8 November 2025; accepted 30 November 2025. Date of publication 5 December 2025; date of current version 25 February 2026. This work was supported in part by the National Natural Science Foundations of China under Grant 52207191, in part by the National Key Research and Development Program of China under Grant 2022YFE0196300, and in part by Science, Technology & Innovation Funding Authority (STDF) under Grant 46505. *(Corresponding author: Yuefei Zuo.)*

Zhan Shen, Qiming Liu, Kaiyuan Liu, Yueyin Wang, and Wu Chen are with the School of Electrical Engineering, Southeast University, Nanjing 210096, China (e-mail: zhs@seu.edu.cn; 220243046@seu.edu.cn; kyliu@seu.edu.cn; yywangee@seu.edu.cn; chenwu@seu.edu.cn).

Jingxin Hu and Yuefei Zuo are with the College of Automation Engineering, Nanjing University of Aeronautics and Astronautics, Nanjing 211106, China (e-mail: jingxin.hu@nuaa.edu.cn; yuefei.zuo@ieee.org).

Frede Blaabjerg and Huai Wang are with the AAU Energy, Aalborg University, 9220 Aalborg, Denmark (e-mail: fbl@energy.aau.dk; hwa@energy.aau.dk).

Color versions of one or more figures in this article are available at https://doi.org/10.1109/TPEL.2025.3640406.

Digital Object Identifier 10.1109/TPEL.2025.3640406

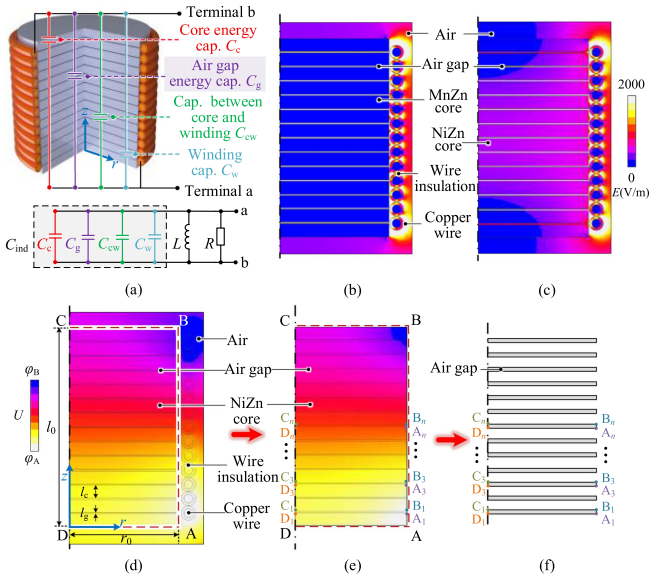

Fig. 1. Stray capacitance of inductors with distributed air gaps. (a) Capacitance difinitions and equivalent circuit. (b) Electric field of gapped MnZn inductor (PEC model holds). (c) Electric field of gapped NiZn inductor (PEC model is not valid). (d) Voltge distribution of gapped NiZn inductor and its simplification to (e) by omitting external winding excitation. (f) Air gap boundary potential analysis.

Conventional ferrite inductors primarily employ MnZn materials (often, permeability $\mu > 1000$ and permittivity $\varepsilon > 10000$) operating within frequency ranges of tens to hundreds of kilohertz. The high permeability originates from the ferrimagnetic order and optimized magnetic anisotropy, while the high permittivity results from interfacial polarization at the insulating grain boundaries. The high permittivity of core leads to its modeling as a perfect electrical conductor (PEC) [3]. This assumption allows for the omission of electric field energy inside the core and its core energy capacitance C_{ce}. Hence, MnZn inductor modeling mainly focuses on winding capacitance C_w [4] and capacitance between core and winding C_{cw} [5], as illustrated in Fig. 1(a).

In recent years, NiZn ferrite cores have gained increasing attention for low-loss characteristic and stable permeability in MHz frequency range. NiZn cores maintain low hysteresis loss at high frequencies and suppress eddy currents due to their high resistivity, thereby significantly reducing core losses [6]. Furthermore, the magnetic field balancing design and distributed air gap structure in NiZn cores can optimize winding losses [7].

Consequently, the use of NiZn materials can significantly reduce overall losses, making it popular in wireless power transfer, power supplies in package, and step-up oscillator applications [6], [7], [8]. Compared to MnZn cores, NiZn cores have lower permeability and permittivity ($4 \lesssim \mu \lesssim 125$, $12 \lesssim \varepsilon \lesssim 100$), resulting in distinct electric field characteristics as compared in Fig. 1(b) and (c). The electric field strength in the core region of the gapped NiZn inductor is comparable to that between the winding and the core. However, due to the larger area of the core region, the electric field energy stored in the core is significantly greater than that between the winding and the core, leading to the non-negligible capacitance C_{ce} and the negligible capacitance C_{cw} [9]. Consequently, traditional MnZn capacitance models, which focus on C_{cw} and neglect C_{ce} are no longer applicable.

To address this, we develop a capacitance model for NiZn cores based on electric field distribution [9], but do not account for air gaps incorporated in practical inductor designs. However, the neglected impact of air gaps leads to parasitic capacitance errors for NiZn gapped inductors. When the core permittivity varies from 12 to 100 in the gapped structure of Case A in Section IV, the errors between the analytical model in [9] and simulation results vary from 27.9% to 206.8%. Hence, it is essential to consider the impact of air gaps when modeling NiZn inductor capacitances.

Existing studies on air gap capacitance mainly focus on MnZn materials. Considering the impact of different air gaps on electric field distribution [10], [11], a multiperfect-electric-conductor assumption is proposed for MnZn core, decomposing the air gap capacitance into plate capacitance, fringe capacitance, and terminal capacitance [12]. For NiZn gapped core inductors, the fringe capacitance and terminal capacitance of both the cores and air gaps are much smaller than the plate capacitance and can be neglected. While the lower permittivity of NiZn materials causes the electric field to penetrate the cores, as shown in Fig. 1(c), making the PEC model inapplicable for the capacitances of both cores and air gaps. Consequently, when calculating the parasitic capacitance of a single-gap NiZn inductor with core radius $r_0 = 15$ mm, core length $l_{\mathrm{c}} = 11$ mm, air gap length $l_{\mathrm{g}} = 1$ mm and core permittivity $\varepsilon_{\mathrm{c}} = 10$, applying the parallel-plate capacitance model from [12] results in a capacitance error up to 190.6% compared with the simulation. The parasitic capacitance error in gapped inductors can lead to the misestimated self-resonant frequency for resonant converters [13]. It also results in unexpected circuit oscillations and voltage spikes that increase switching losses, misguides EMI filter design, and increases system size and cost.

To address this issue, this article proposes two air gap capacitance models for NiZn inductors. They are generic for different air gap positions, numbers, sizes, and boundary conditions. Both models are verified by finite element simulations and experiments in six case.

II. Analytical Modeling of Boundary Potential

A. Model Simplification of Gapped Core Inductor

The 3-D model of the distributed gapped inductor is illustrated in Fig. 1(a), it is simplified to 2-D in Fig. 1(d), and is further simplified to Fig. 1(e), with the simplification of the winding section. The voltage across the winding can be assumed to change linearly along z-axis direction, and the core surface is wrapped by the winding closely. Hence, the voltage distribution of the core surface matches the linear profile, i.e., the boundary AB of core follows a linear potential distribution in Fig. 1(e). The electric field potential of the cores and air gaps φ follows Laplace's equation as follows:

$$\nabla^2 \varphi = 0. \tag{1}$$

The analytical modeling of boundary potential of the air gap is the basis for solving Laplace's equation. It is also used for calculating the electric field distribution and the capacitance of the gapped core. The boundary potential condition is determined by the voltage along the core AB, BC, and AD in Fig. 1(e), and along the air gaps $\mathrm{A}_1\mathrm{D}_1$, $\mathrm{A}_2\mathrm{D}_2$, … $\mathrm{A}_n\mathrm{D}_n$, $\mathrm{B}_1\mathrm{C}_1$, $\mathrm{B}_2\mathrm{C}_2$, … $\mathrm{B}_n\mathrm{C}_n$ in Fig. 1(f). Boundary AB is the same as winding voltage, the core boundary potential AD, BC are given in [9]. For NiZn gapped cores, the distributed air gaps and the low permittivity characteristic of the NiZn cores increase the difficulty in determining the boundary potential. Hence, the key problem is to solve the voltage distribution of the air gap boundary $\mathrm{A}_n\mathrm{D}_n$ and $\mathrm{B}_n\mathrm{C}_n$, respectively. In the following Section II-B and II-C, two methods for boundary solutions of air gaps are proposed: the multilayer dielectric model and the potential superposition model, respectively.

B. Boundary Solution 1: Multilayer Dielectric Model

The simplified gapped core is a multilayer dielectric structure, which comprises stacked homogeneous dielectric layers with constant permittivity. For adjacent air gap layer and core layer, their interlayer boundary $\mathrm{A}_n\mathrm{D}_n, \mathrm{B}_n\mathrm{C}_n$ at $z = z_{\mathrm{i}}$ satisfy continuity conditions on both electric potential and normal component of the electric displacement as follows:

$$\varphi_{\mathrm{c}}(r, z_{\mathrm{i}}) = \varphi_{\mathrm{g}}(r, z_{\mathrm{i}}) \tag{2}$$

$$\varepsilon_{\mathrm{c}} \frac{\partial \varphi_{\mathrm{c}}(r,z)}{\partial z}\bigg|_{z=z_{\mathrm{i}}} = \varepsilon_{\mathrm{g}} \frac{\partial \varphi_{\mathrm{g}}(r,z)}{\partial z}\bigg|_{z=z_{\mathrm{i}}} \tag{3}$$

where φ_{c} and φ_{g} represent the electric potential of the core and the air gap, respectively, ε_{c} and ε_{g} are their corresponding relative permittivity. The boundary condition along the core surface at $r = r_0$ fundamentally governs unidirectional linear potential distributions along the z-axis within dielectric layers, thereby establishing a uniform normal potential gradient throughout each dielectric layer. Equation (3) indicates that the normal potential gradient at the interlayer boundary between adjacent core and air gap is inversely proportional to the relative permittivity, with a discontinuous transition across the boundary. Fig. 2 shows the potential distribution of the core and the air gap with the relative permittivity of 10 and 1, respectively, which validates the discussion of (3). Consequently, the generalized governing equation for arbitrary radial coordinates can be derived as follows:

$$N_{\mathrm{c}} l_{\mathrm{c}} \frac{\partial \varphi_{\mathrm{c}}}{\partial z}(r) + N_{\mathrm{g}} l_{\mathrm{g}} \frac{\partial \varphi_{\mathrm{g}}}{\partial z}(r) = 2\varphi_{\mathrm{L}}(r) \tag{4}$$

where N_{c} and N_{g} denote the number of magnetic cores and air gaps, l_{c} and l_{g} are core and air gap layer length, $\partial\varphi_{\mathrm{c}}/\partial z$

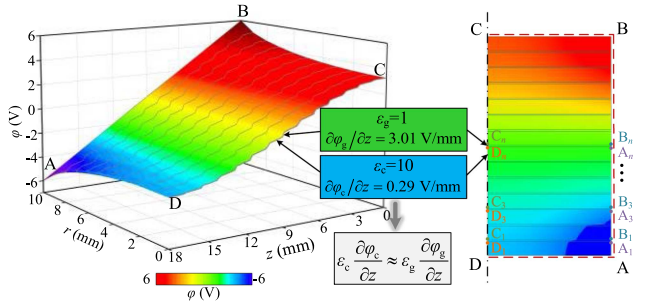

Fig. 2. Potential distribution of 2-D gapped core model with $\varepsilon_c = 10$ and $\varepsilon_g = 1$.

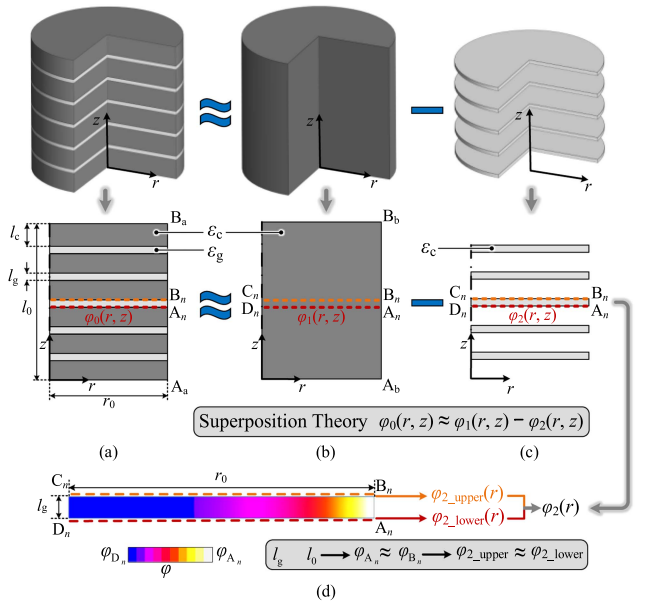

Fig. 3. Potential superposition model. (a) Gapped core model. (b) Core model without air gap. (c) Air gap model with a relative permittivity of ε_c. (d) Potential distribution of the single air gap model.

(r) and $\partial\varphi_g/\partial z$ (r) are the gradient of the potential along the z-axis direction across the core layers and the air gap layers, respectively. $\varphi_L(r)$ obtained from [9] indicates the boundary potential of core at $z = 0$. Hence, the potential of the upper boundary B_nC_n and lower boundary A_nD_n of the nth air gap along the z-axis direction $\varphi_{upper}(r)$ and $\varphi_{lower}(r)$ can be determined, respectively, as follows:

$$\varphi_{upper}(r) = \varphi_L(r) - nl_c\frac{\partial\varphi_c}{\partial z}(r) - nl_g\frac{\partial\varphi_g}{\partial z}(r) \quad (5)$$

$$\varphi_{lower}(r) = \varphi_L(r) - nl_c\frac{\partial\varphi_c}{\partial z}(r) - (n-1)\,l_g\frac{\partial\varphi_g}{\partial z}(r). \quad (6)$$

C. Boundary Solution 2: Potential Superposition Model

Laplace's equation is a linear homogeneous partial differential equation, where the superposition of solutions remains valid under homogeneous boundary conditions. We propose to use the superposition principle to obtain potential boundary conditions of air gaps, which includes following five steps.

1) For gapped core as shown in Fig. 3(a), we define a core of the same shape but without gap in Fig. 3(b). The voltage at the surface of the core in Fig. 3(b) is set to twice that of Fig. 3(a), i.e., $\varphi_{Ab} = 2\varphi_{Aa}$, $\varphi_{Bb} = 2\varphi_{Ba}$.
2) In Fig. 3(b), the potential at the same positions as the upper and lower boundaries of the air gap in Fig. 3(a) are denoted as $\varphi_1(r, z)$ using dashed lines. $\varphi_1(r, z)$ is determined through a general NiZn core model given in [9].
3) In Fig. 3(c), a model with the same air gap in Fig. 3(a), but with a permittivity of ε_c is established. Apply the same linear voltage from points A_n to B_n in Fig. 3(c) as from those in Fig. 3(a), the potential of the corresponding boundaries of the air gap in Fig. 3(c) are denoted as $\varphi_2(r, z)$.
4) Subtract boundary potential in Fig. 3(c) $\varphi_2(r, z)$ from Fig. 3(b) $\varphi_1(r, z)$, leading to the boundary condition of Fig. 3(a) $\varphi_0(r, z) \approx \varphi_1(r, z) - \varphi_2(r, z)$. Hence, Fig. 3(a)'s boundary condition is obtained by the superposition of Fig. 3(b) and (c).
5) An air gap model with permittivity ε_c is in Fig. 3(d). Its length l_g is negligible compared to total core length l_0. Therefore, the voltage excitation at point A_n approximates that at point B_n, resulting in similar potential at the upper and lower boundaries, $\varphi_{2\_upper}(r) \approx \varphi_{2\_lower}(r)$.

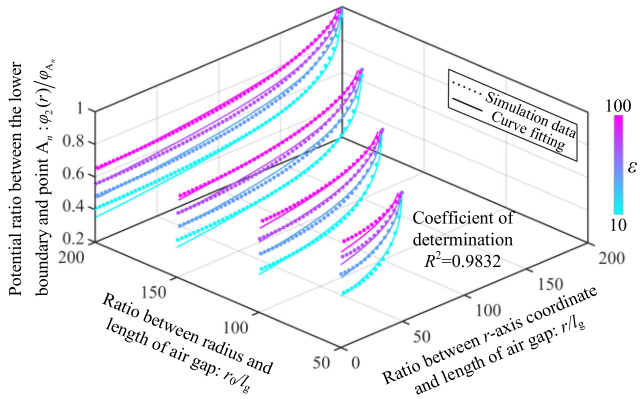

Fig. 4. 4-D curve fitting results of $\varphi_2(r)/\varphi_{An}$.

The lower boundary potential $\varphi_2(r)$ under different r_0/l_g ratios and ε_c values is obtained in Fig. 4 by finite element simulation, and an analytic relationship is obtained as follows:

$$\varphi_2(r) = 1.2989\varphi_{A_n}e^{-0.6468\varepsilon_c^{-0.2642}\frac{[(r_0-r)}{l_g^{0.2478}}}. \quad (7)$$

It achieves a coefficient of determination $R^2 = 0.9832$, which demonstrates a good agreement with simulation.

D. Boundary Solution Verification

A case study of a gapped core inductor is designed to verify the proposed two boundary solutions, as shown by the comparison of finite element analysis and analytical calculation in Fig. 5. It is with core radius $r_0 = 10$ mm, core length $l_0 = 20$ mm, air gap length $l_g = 0.1$ mm, number of air gaps $N_g = 13$, and core permittivity $\varepsilon_c = 10$.

Comparative analysis reveals that Solutions 1 and 2 demonstrate a slightly larger error from simulations when r approaches

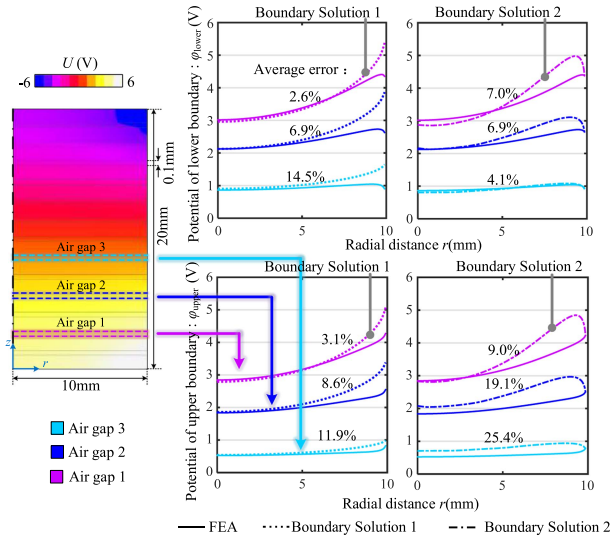

Fig. 5. Simulation verification of Boundary Solutions 1 and 2.

r_0. In Solution 1, the different relative permittivities of the dielectric layers cause a sudden change in the normal gradient of the potential at the interlayer boundary, and it remains stable along the z-axis within the same dielectric layer. However, as r gets closer to r_0, the influence of the applied linear voltage at $r = r_0$ increases, the boundary potential error between Solution 1 and simulation becomes larger with the overestimation of the normal potential gradient, especially for relatively high-permittivity NiZn cores. The boundary potential error in Solution 2 primarily stems from its two superimposed submodels. First, in the core model without air gap, the curve fitting of the boundary potential from [9] demonstrates insufficient accuracy under the condition $r_0 < l_0$. Second, in the air gap model, the fringing effect of the electric field causes the assumption $\varphi_{2\_upper}(r) \approx \varphi_{2\_lower}(r)$ to become inadequate in regions where r approaches r_0. Nevertheless, the errors of both solutions are below 20% and fall within an acceptable range for capacitance calculation [5], [9], [12].

Solution 1 provides an efficient, general-purpose analytical model with less reliance on fitting simulation data but has inherent errors for relatively high-permittivity NiZn cores. In contrast, Solution 2 accounts for the combined effects of key structural parameters in gapped cores through simulation-based modeling. However, Solution 2 requires higher computational complexity and has limited applicability beyond its fitted parameter range. The choice between them can be made based on the requirements of the application.

III. Analytical Model of Energy Capacitance

By solving Laplace's equation under the proposed two air gap boundary conditions, the potential distribution in the core and air gap $\varphi(r, z)$ can be obtained. The detailed procedures are given in Appendix A. The overall analytical modeling procedure is summarized in Fig. 6. The electric field strength is calculated by

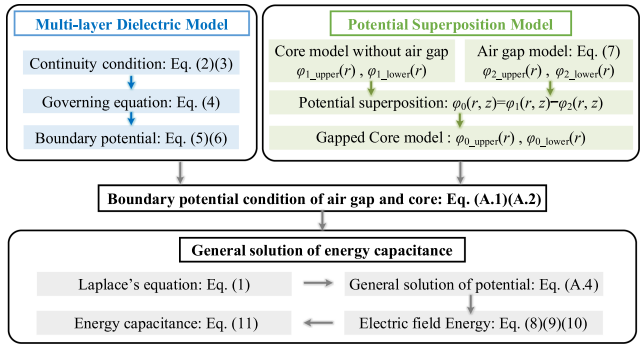

Fig. 6. Analytical model of the energy capacitance of gapped core.

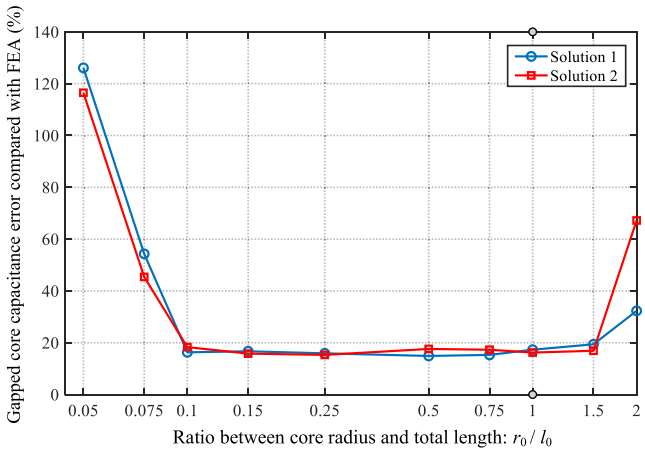

Fig. 7. Gapped core capacitance error over $\log_2(r_0/l_0)$ coordinate with r_0/l_0 ratios ranging from 0.05 to 2.

the negative gradient of the electric potential as follows:

$$|E| = \sqrt{\left(-\frac{\partial\varphi(r,z)}{\partial r}\right)^2 + \left(-\frac{\partial\varphi(r,z)}{\partial z}\right)^2}. \tag{8}$$

The electric field energy of each air gap layer and core layer W_g and W_c can be obtained using following integration:

$$W_g = \frac{1}{2}\varepsilon_0\varepsilon_g \int_0^{r_0}\int_0^{l_g} \pi r|E|^2 dr dz \tag{9}$$

$$W_c = \frac{1}{2}\varepsilon_0\varepsilon_c \int_0^{r_0}\int_0^{l_c} \pi r|E|^2 dr dz. \tag{10}$$

The total energy of the gapped core W_{gc} is obtained by adding up the electric field energy of each part, and the total energy capacitance of the gapped core C_{gc} is as follows:

$$C_{gc} = \frac{2W_{gc}}{\Delta U^2} \tag{11}$$

where ΔU is the voltage across the winding, approximately equivalent to twice the potential at point Aa in Fig. 3(a).

To determine the applicable range of dimensional values of the proposed models, ten NiZn gapped core cases are studied with r_0/l_0 ratios ranging from 0.05 to 2, core radius $r_0 = 1$ mm, air gap length $l_g = 0.01$ mm, core permittivity $\varepsilon_c = 10$, and number of air gaps $N_g = 4$. The gapped core capacitance errors variation with the r_0/l_0 ratios is shown in Fig. 7. For structures

TABLE I
Parameters of Inductors in Six Cases

Parameter	Case A	Case B	Case C	Case D	Case E	Case F
Core/air gap radius r_0 (mm)	25	25	25	25	17.5	15
Total length l_0 (mm)	46.6	51.6	71.2	71.2	76.6	71.2
Core length l_c (mm)	5	10	10	10	15	10
Air gap length l_g (mm)	0.2	0.4	0.2	0.2	0.4	0.2
Number of cores N_c	9	5	7	7	5	7
Number of air gaps N_g	8	4	6	6	4	6
Core permittivity ε	15.0	15.0	15.0	10.5	10.5	5.7
Wire diameter d_i (mm)	0.9	0.9	1.0	1.0	1.0	0.9
Number of turns N_i	44	44	50	50	57	57

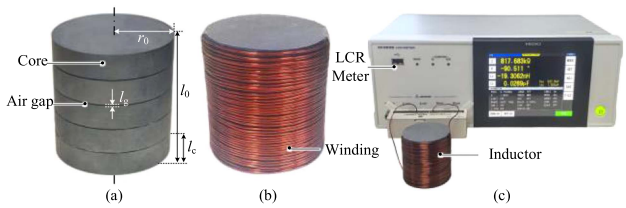

Fig. 8. Experimental cases and test instruments. (a) Gapped core. (b) Inductor. (c) Experimental instruments.

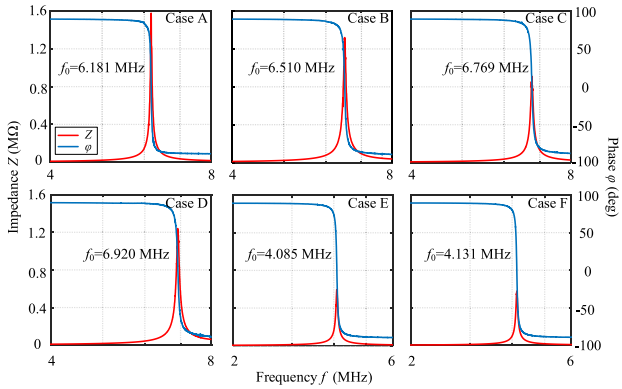

Fig. 9. Measured impedance and phase of six cases.

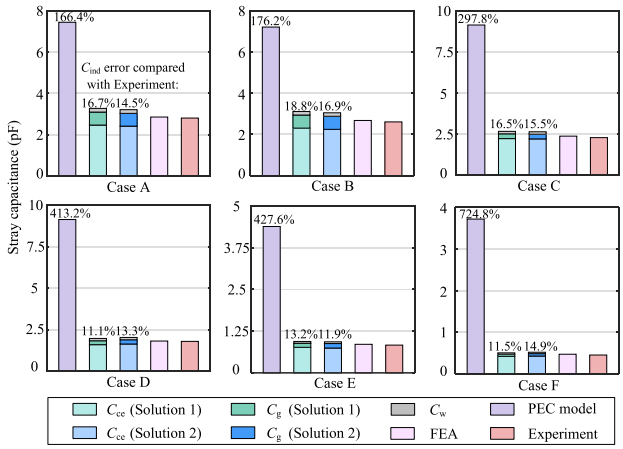

Fig. 10. Verification through experiments and simulations of six cases.

with the ratio $r_0/l_0 < 0.1$, the extremely small r_0 relative to l_0 results in negligible radial variation of the potential at the upper and lower boundaries of air gaps and cores, and causes relatively large errors in gapped core capacitance. For structures with the ratio $r_0/l_0 > 1.5$, the significant fringing effect near $r = r_0$ becomes the dominant factor for electric field distribution and capacitance. Both Solution 1 and Solution 2 have relatively high errors as r approaches r_0, resulting in overestimated gapped core capacitance. With the error of less than 20% as the acceptable range for capacitance calculation [5], [9], [12], the results demonstrate that the reasonable range of ratio between core radius and total core length r_0/l_0 for both Solution 1 and Solution 2 is from 0.1 to 1.5. The r_0/l_0 ratios of rod NiZn cores for engineering production in most manufacturers fall within the applicable range of our proposed models, with values predominantly concentrated between 0.1 and 0.3 [14], [15], [16], [17]. Therefore, the applicable range of dimensional values of our analytical models is reasonable.

IV. Experimental Verification

Six cases A, B, C, D, E, and F of NiZn inductors with uniformly distributed air gaps are designed for experimental verification as shown in Fig. 8, with detailed parameters given in Table I. The measurements are performed using a Hioki IM 3536 *LCR* meter and results are shown in Fig. 9. The parasitic capacitance C_{ind} is calculated from first-resonant frequency f_0 and inductance value L by $C_{\text{ind}} = \frac{1}{L(2\pi f_0)^2}$. Cases E and F have lower capacitance values and therefore we connect a 5.2-pF capacitor in parallel to reduce the resonant frequency. The winding-related capacitance C_w is calculated by [4], while the air-gap-related capacitance C_g and the core-related capacitance C_{ce} are obtained using our proposed models. Adding them together obtains analytically calculated C_{ind}. The analytical errors compared with experiments are shown in Fig. 10.

Cases A and B have identical total length of air gaps and Consequently, they demonstrate comparable air gap capacitance and core capacitance. In contrast, Case C shares the same single air gap length l_g as Case A but features a reduced number of air gaps and a lower ratio of r_0/l_0, leading to a significant decrease in air gap capacitance. Case D differs from Case C in its lower relative permittivity with all other parameters identical, and it has a reduced stray capacitance. The smaller total capacitance values in Cases E and F compared with those in Cases A, B, and C are caused by their smaller core radii, greater total lengths, and lower core relative permittivities.

The average errors of the total capacitance in six cases solved by Solutions 1 and 2 are 14.6% and 14.5%, respectively, mainly stemming from the overestimation of the potential values in the region where r approaches r_0 in both boundary solutions, and

V. Conclusion

An analytical stray capacitance model of NiZn core inductor with air gaps is proposed and verified by simulations and experiments in six cases. The air gap capacitance accounts for a proportion ranging from 9.9% to 20.7% of the total stray capacitance, which cannot be neglected in the modeling. The average errors of the air gap capacitance solved by Solutions 1 and 2 are 12.8% and 13.6%, respectively.

Appendix A
Derivation of the Potential of Air Gaps and Cores

Sequentially numbering air gaps and cores along the z-axis as $n = 1, 2, \ldots, N_{\mathrm{g}}$ and $n = 0, 1, \ldots, N_{\mathrm{g}}$, the boundary conditions of each layer of air gaps and cores are determined, respectively, as follows:

$$\begin{cases} \varphi_{\mathrm{g}}\left|_{z=0}\right. = \varphi_{\mathrm{lower}}\left(r, z = n\left(l_{\mathrm{c}} + l_{\mathrm{g}}\right) - l_{\mathrm{g}}\right) \\ \varphi_{\mathrm{g}}\left|_{z=l_{\mathrm{g}}}\right. \varphi_{\mathrm{upper}}\left(r, z = n\left(l_{\mathrm{c}} + l_{\mathrm{g}}\right)\right) \\ \varphi_{\mathrm{g}}\left|_{r=r_0}\right. = \varphi_{\mathrm{A}_0}\left\{1 - 2^{\frac{[n(l_{\mathrm{c}}+l_{\mathrm{g}})-l_{\mathrm{g}}+z]}{l_0}}\right\} \\ n = 1,\ 2,\ \ldots, N_{\mathrm{g}} \end{cases} \tag{A.1}$$

$$\begin{cases} \varphi_{\mathrm{c}}\left|_{z=0}\right. = \varphi_{\mathrm{upper}}\left(r, z = n\left(l_{\mathrm{c}} + l_{\mathrm{g}}\right)\right) \\ \varphi_{\mathrm{c}}\left|_{z=l_{\mathrm{c}}}\right. = \varphi_{\mathrm{lower}}\left(r, z = (n+1)\left(l_{\mathrm{c}} + l_{\mathrm{g}}\right) - l_{\mathrm{g}}\right) \\ \varphi_{\mathrm{c}}\left|_{r=r_0}\right. = \varphi_{\mathrm{A}_0}\left\{1 - 2^{\frac{[n(l_{\mathrm{c}}+l_{\mathrm{g}})+z]}{l_0}}\right\} \\ n = 0,\ 1,\ \ldots, N_{\mathrm{g}}. \end{cases} \tag{A.2}$$

Let the original potential distribution subtracts $\varphi \,|\, r = r_0$, the boundary condition and problem transfer to

$$\begin{cases} \varphi'\left|_{z=0}\right. = \varphi\left|_{z=0}\right. - \varphi\left|_{r=r_0}\right. \\ \varphi'\left|_{z=l}\right. = \varphi\left|_{z=l}\right. - \varphi\left|_{r=r_0}\right. \\ \varphi'\left|_{r=r_0}\right. = 0 \\ \nabla^2\varphi' = 0. \end{cases} \tag{A.3}$$

The parameter l represents the core length l_{c} when solving core sections, and represents the air gap length l_{g} when solving air gap sections, respectively. The general solution can be obtained as follows [18]:

$$\varphi' = A_0 + B_0 z + \sum_{n=1}^{\infty}\left(A_n e^{x_n^{(0)} z/r_0} + B_n e^{-x_n^{(0)} z/r_0}\right) \cdot J_0\left(\frac{x_n^{(0)}}{r_0} r\right) \tag{A.4}$$

where the nth positive zero of J_1 is denoted by $x_{\mathrm{n}}{}^{(0)}$, J_0 and J_1 represent the Bessel functions of the first kind with orders 0 and 2, A_0, B_0, A_{n}, and B_{n} are all coefficients to be determined. Combing the boundary conditions obtains

$$\begin{cases} A_0 = 0, \quad A_n = \frac{G_{1n} e^{-x_n^{(0)} l/r_0} - G_{2\mathrm{n}}}{e^{-x_n^{(0)} l/r_0} - e^{x_n^{(0)} l/r_0}} \\ B_0 = 0, \quad B_n = \frac{G_{1n} e^{x_n^{(0)} l/r_0} - G_{2\mathrm{n}}}{e^{x_n^{(0)} l/r_0} - e^{-x_n^{(0)} l/r_0}} \\ G_{1n} = \frac{2}{r_0^2\left[J_0\left(x_n^{(0)}\right)\right]^2}\int_0^{r_0} \varphi'\left|_{z=0}\right. J_0\left(\frac{x_n^{(0)}}{r_0} r\right) r dr \\ G_{2n} = \frac{2}{r_0^2\left[J_0\left(x_n^{(0)}\right)\right]^2}\int_0^{r_0} \varphi'\left|_{z=l}\right. J_0\left(\frac{x_n^{(0)}}{r_0} r\right) r dr. \end{cases} \tag{A.5}$$

The final solution of $\varphi(r, z)$ is as follows:

$$\varphi\left(r, z\right) = \varphi'\left(r, z\right) + \varphi\left|_{r=r_0}\right.. \tag{A.6}$$

References

[1] H. Zhao et al., "Parasitic capacitance modeling of copper-foiled medium-voltage filter inductors considering fringe electrical field," *IEEE Trans. Power Electron.*, vol. 36, no. 7, pp. 8181–8192, Jul. 2021.

[2] C. Fei, Y. Yang, Q. Li, and F. C. Lee, "Shielding technique for planar matrix transformers to suppress common-mode EMI noise and improve efficiency," *IEEE Trans. Ind. Electron.*, vol. 65, no. 2, pp. 1263–1272, Feb. 2018.

[3] I. V. Lindell and A. H. Sihvola, "Transformation method for problems involving perfect electromagnetic conductor (PEMC) structures," *IEEE Trans. Antennas Propag.*, vol. 53, no. 9, pp. 3005–3011, Sep. 2005.

[4] J. Biela and J. W. Kolar, "Using transformer parasitics for resonant converters—A review of the calculation of the stray capacitance of transformers," *IEEE Trans. Ind. Appl.*, vol. 44, no. 1, pp. 223–233, Jan./Feb. 2008.

[5] Z. Shen, H. Wang, Y. Shen, Z. Qin, and F. Blaabjerg, "An improved stray capacitance model for inductors," *IEEE Trans. Power Electron.*, vol. 34, no. 11, pp. 11153–11170, Nov. 2019.

[6] D. Etta, S. S. Rashid, S. Maji, and K. K. Afridi, "Design of low-loss magnetic-core toroidal inductor for multi-MHz wireless power transfer systems," in *Proc. 2024 IEEE Workshop Control Model. Power Electron.*, Lahore, Pakistan, 2024, pp. 1–6.

[7] H. T. Le et al., "High-Q three-dimensional microfabricated magnetic-core toroidal inductors for power supplies in package," *IEEE Trans. Power Electron.*, vol. 34, no. 1, pp. 74–85, Jan. 2019.

[8] E. Macrelli et al., "Modeling, design, and fabrication of high-inductance bond wire microtransformers with toroidal ferrite core," *IEEE Trans. Power Electron.*, vol. 30, no. 10, pp. 5724–5737, Oct. 2015.

[9] Z. Shen et al., "Core energy capacitance of NiZn inductors," *IEEE Trans. Power Electron.*, vol. 38, no. 4, pp. 4235–4240, Apr. 2023.

[10] S. Luan and H. Zhao, "Electric-field analyses of airgaps in magnetic cores," in *Proc. 2023 IEEE Energy Convers. Congr. Expo.*, Nashville, TN, USA, 2023, pp. 5639–5644.

[11] S. Luan, M. Duffy, and H. Zhao, "Trade-off design of gap formats in magnetic components," in *Proc. IEEE 2nd Int. Power Electron. Application Symp.*, Guangzhou, China, 2023, pp. 590–594.

[12] S. Luan, Z. Yan, and H. Zhao, "Effects of airgaps on parasitic capacitance of magnetic components," *IEEE Trans. Power Electron.*, vol. 39, no. 1, pp. 1115–1134, Jan. 2024.

[13] B. Xie, Q. Li, Y. Zhang, and C. Yuan, "High-frequency electromagnetic behavior, impedance modeling, and enhancement of low-permeability powder cores," *IEEE Trans. Power Electron.*, vol. 40, no. 2, pp. 3336–3356, Feb. 2025.

[14] Chinadmegc, "Z cores," 2022, Accessed: Oct. 26, 2025. [Online]. Available: https://chinadmegc.com/uploads/20221025/bf98ffd65e5c8f8ec525db2b068cc3a7.pdf

[15] Fair-Rite Products Corp., "Applied filters," 2025, Accessed: Oct. 26, 2025. [Online]. Available: https://fair-rite.com/parametric-search/

[16] New conda, "Rod cores," 2023, Accessed: Oct. 26, 2025. [Online]. Available: http://www.ncd.com.cn/companyfile/71.html

[17] Ferroxcube, "Product specifications - rod cores,", 2016, Accessed: Oct. 26, 2025. [Online]. Available: https://www.ferroxcube.com/upload/media/product/file/Pr_ds/rod.pdf

[18] M. Zahn, *Electromagnetic Field Theory: A Problem Solving Approach*. Malabar, FL, USA: Krieger Publishing, 2003.